Jurnal Kejuruteraan 38(1) 2026: 465-483
https://doi.org/10.17576/jkukm-2026-38(1)-40

4-Port High-Gain Metamaterial-Inspired Element-Based MIMO Antenna Array for 5G mmWave Applications

Noor Al-Bandar[a*],Mandeep Jit Singh[a,b*], Mohammad Tariqul Islam[a], Samir Salem Al-Bawri[b] & Husam Hamid Ibrahim[c]

[a]*Department of Electrical, Electronic and Systems Engineering, Faculty of Engineering and Built Environment, Universiti Kebangsaan Malaysia UKM Bangi 43600, Selangor, Malaysia*

[b]*Space Science Centre, Climate Change Institute, Universiti Kebangsaan Malaysia (UKM), Bangi 43600, Malaysia*

[c]*Department of Computer Engineering Techniques, Bilad Alrafidain University College, Diyala, 32001, Iraq*

[*]*Corresponding authors: p117813@siswa.ukm.edu.my; mandeep@ukm.edu.my*

Received 10 June 2025, Received in revised form 30 September 2025
Accepted 30 October 2025, Available online 30 January 2026

ABSTRACT

Millimeter-wave 5G devices need compact MIMO arrays that provide high gain while minimizing inter-port coupling; conventional arrays struggle to balance gain, bandwidth, and isolation in small footprints.This article discusses a compact, high-performance four-port orthogonal MIMO antenna system for millimeter-wave 5G uses that works in bands n257(26.50–29.50 GHz), n258(24.25–27.50 GHz), and n261(27.50–28.35 GHz). Each of the four ports has a 4x4 sub-array with a total of 16 elements (individual element small size with dimensions of 0.32λ0×0.26λ0 excluding feed), along with a 13x10 double-negative (DNG) metamaterial reflector. The antenna is built on a Rogers 5880 substrate, which is well-known for having great dielectric characteristics. The antenna has dimensions of 4.86λ_0× 4.81λ_0× 0.073λ_0, but it has a high gain of 14.3 dBi, a wide spread of 8.06 GHz, and a 97% radiation efficiency. Adding metamaterials that have negative permittivity, permeability, and refractive index greatly improves performance by getting excellent isolation of more than -32.7 dB and increasing the bandwidth by 200 MHz. The metamaterial's unit cell was modeled with CST and validated by showing an identical circuit in ADS. A prototype antenna design was Fabricated and measured and the results were closely matched the simulations. Five machine-learning regression models were also used to verify and evaluate the antenna's performance, including its gain. Support Vector Regression (SVR) and Extreme Gradient Boosting (XGB) methods were the most accurate, with 96% or more prediction accuracy. The results show that the suggested MIMO antenna system based on metamaterials works well and can be used in real-life 5G scenarios.

Keywords: MIMO antenna; antenna array; 5G; metamaterial; gain, ML.

INTRODUCTION

In an era marked by an explosive flow in annual data traffic, ranging from 40% to 70%, the future demands on wireless networks are projected to increase by an astonishing factor of 1000 compared to current requirements. To confront this monumental challenge, fifth-generation (5G) systems have emerged as a formidable solution, offering multi-gigabit-per-second (Gb/s) peak throughput, positioning themselves as the linchpin for future communication applications (Tariq et al. 2021). The constraints on capacity and bandwidth of channels operating below 6 GHz have led academic scholars and engineers to explore the unused mm-wave spectrum as a potential solution for implementing fifth-generation wireless communication systems (Rai et al. 2023; Singh et al. 2023). The significance of 5G technology transcends the fulfillment of burgeoning data rate demands. It expands its impact to tackle challenges related to low power consumption, reliability, and scalability arising from the rapidly growing number of connected devices. Furthermore, it acts as a driving force for emerging technological advancements such as smart

cities, the Internet of Vehicles (IoV), and virtual reality (Rappaport et al. 2013). Nevertheless, this progress comes with a condition, as the utilization of the mm-Wave spectrum brings about certain challenges that affect signal quality, such as atmospheric absorption and attenuation due to path loss (Banday et al. 2019). Thus, the allocation of frequency bands assumes paramount importance in modeling effective communication systems, a concern that has spurred worldwide efforts by telecom regulatory bodies and industry leaders to standardize 5G communication networks. An overview of mm-wave spectrum allocation globally reveals a prevailing preference for the 26/28 GHz frequency band(Imam-Fulani et al. 2023).

The backbone of successful communication networks lies in the design and deployment of antennas. In the realm of 5G systems, set to deploy multiple antennas at both base stations and user terminals, Antennas become necessary elements, playing a key role in 5G millimeter-wave communication. Key factors that facilitate this include the use of antenna arrays, MIMO technology, and beamforming methods(Song et al. 2017). Recent research has explored a multitude of antenna configurations customized for the potential of mm-Wave bands (Al-Bawri et al. 2024; Bang & Choi 2018; Mandloi et al. 2023; Mulla et al. 2021; Omar et al. 2024; Pozar ; Sultan et al. 2020).Intensive research has been conducted on high-gain antenna arrays with beamforming capabilities to enhance signal strength and expand spatial coverage (Bang & Choi 2018; Mandloi et al. 2023). It is crucial to acknowledge that augmenting the quantity of radiators in an array improves antenna gain. Nonetheless, larger array configurations might experience losses in the power dividers. As a result, there is an increasing focus on creating high-gain antennas that have a minimal profile. This involves designs such as antennas utilizing metamaterials (Omar et al. 2024). Furthermore, to support the capacity of the communication system, MIMO technology emerges as a necessary tool, allowing multiple antennas to operate simultaneously. This advancement significantly enhances data rates, overall capacity, and communication link reliability (Al Abbas et al. 2019; El-Nady et al. 2021; Mulla et al. 2021; Pozar; Sultan et al. 2020). Noteworthy breakthroughs include the introduction of bi-layered Frequency Selective Surface (FSS) superstrates to address mutual coupling effects, thereby achieving substantial improvements in isolation. Additionally, techniques such as metamaterial-based corrugations have been implemented to reduce coupling between MIMO antennas, achieving notable isolation enhancements (Sehrai et al. 2021).

While metamaterials show promise in improving antenna performance, there is an ongoing drive to strike an optimal balance between gain enhancement and isolation improvement, recognizing the paramount importance of both factors for efficient antenna performance. The work in (Mulla et al. 2021), suggests a millimeter-wave massive MIMO system designed for a single user, and the implementation involves the utilization of a defected ground structure alongside a square array of patch antennas constructed of metamaterials. The system, characterized by its compact dimensions, functions at a frequency of 28 GHz, possesses a bandwidth spanning 3.1 GHz, and attains a gain of around 6.28 dBi. Likewise, in(Murthy 2020), an alternative method is introduced to reduce coupling between MIMO antennas. In other recent studies, have been on how to improve MIMO output using metamaterials. In (El Houda Nasri et al. 2024), Presenting a metamaterial that incorporates a 4x4 MIMO antenna featuring circular polarization at a frequency of 28 GHz. This design utilizes square split ring resonators and possesses dimensions of 45.5 x 45.5 x 0.8. The bandwidth of this metamaterial spans from 24.3 to 30.9 GHz, while maintaining isolation levels below -25 dB.

In Iqbal et al. (2019), A mm-wave MIMO antenna with two ports is documented, incorporating an Electromagnetic Band Gap (EBG) structure to enhance gain. Integrating EBG leads to a gain enhancement of 1.9 dBi, reaching a maximum gain of 6 dBi. The design proposed in(Saad & Mohamed 2019), demonstrated in the study, specified the application of An Electromagnetic Band-Gap (EBG) reflector placed beneath a a MIMO antenna with two ports to augment the antenna's gain. A peak gain of 11.5 dBi was achieved by the proposed geometry The antenna exhibits effective MIMO capabilities alongside significant gain, its overall structure has relatively large dimensions, limiting its compatibility with forthcoming miniaturized communication devices. Nonetheless, the antenna is relatively large in size and if expanded to a a MIMO configuration with four ports from its original two-port configuration, the size will further grow, accompanied by a reduction in the achieved operational bandwidth. In light of the constraints elucidated in previous discussions regarding antenna designs, this study advocates the implementation of a 16-element Multiple Input Multiple Output (MIMO) antenna tailored specifically for millimeter-wave (mm-wave) 5G communication devices. Emphasizing both compact antenna dimensions and performance enhancement, the integration of a metamaterial (DNG reflector) exhibiting double negative characteristics is proposed. This inclusion aims to augment gain, bandwidth, and isolation properties. To elevate gain performance, a singular antenna element undergoes transition into an array configuration, resulting in each MIMO antenna comprising a 4×4 array of elements, all energized by a parallel feeding network. The rationale behind this approach is to further amplify gain while simultaneously mitigating interference among MIMO

elements. Situated strategically beneath the MIMO elements lies a rectangular plate housing a 13×10 array of DNG reflector with double negative elements. Operational within the mm-wave frequency spectrum spanning 25.94-34 GHz, aligning with radiation bands designated within the 5G millimeter wave frequency band n257, the proposed antenna showcases notable gain enhancement, with peak gain reaching 14.3 dBi. Furthermore, the incorporation of the DNG reflector yields improvements in isolation, gain, and bandwidth characteristics.

THE DESIGN AND CONSTRUCTION PROCESS OF ANTENNAS

The proposed antenna design is an innovative arrangement consisting of 16 elements in a MIMO configuration. The objective is to enhance the effectiveness of wireless communication systems by increasing their efficiency. The chosen substrate for this design is Rogers RT/Duroid 5880, known for its favorable attributes in high-frequency applications. The substrate has a size of 51.6× 52.2 mm2, providing sufficient space for accommodating the antenna elements and other components. Rogers RT/Duroid 5880 offers excellent electrical properties, The dielectric constant (εr) of 2.2 has an impact on how electromagnetic waves propagate within the substrate, affecting the antenna's characteristics such as impedance matching and radiation efficiency. The substrate also has a thickness (h) of 0.787 mm, which contributes to the overall compactness and thickness of the antenna design. To ensure proper full ground and minimize undesired radiation, a copper ground plane is employed to back the substrate. Copper is a common choice for its excellent electrical conductivity and suitability for high-frequency applications. Providing a solid grounding plane helps reduce electromagnetic interference and improve the overall performance of the antenna system. In addition to the MIMO antenna structure and substrate configuration, an essential component integrated into the design is the DNG reflector unit cells. These unit cells are strategically positioned below the MIMO antennas, approximately 0.465 λ the distance from the antennas. Metamaterials exhibit unique electromagnetic properties not found in natural materials, facilitating the manipulation of wave propagation characteristics. The antenna design incorporates Conformal Substrate Integrated Waveguide (CSIW) cells to improve performance in terms of bandwidth, gain, and radiation pattern, which constitutes the primary objective. The configuration is replicated and simulated using the commercially available electromagnetic (EM) simulator, CST Microwave Studio. Figure 1 illustrates the successive stages of the design process. Subsequent sections provide an in-depth exploration of the stepwise design methodology, the optimization techniques employed, and the corresponding results. Figure 2 showcases the prototype of the proposed design.

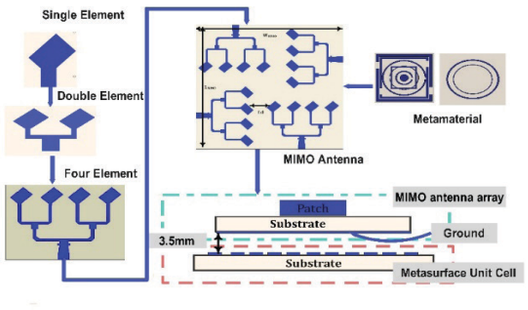

FIGUR1.The steps of the proposed antenna are loaded with metamaterial.

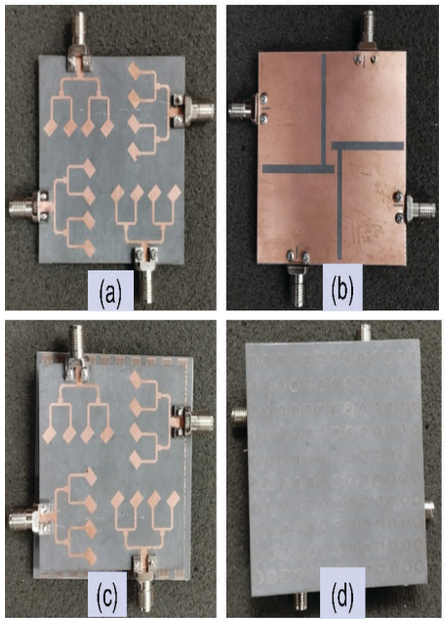

FIGURE 2. Depicts the prototype of the suggested design, showing the (a) front;(b) back;(c) front and (d) back .

DESIGN OF METAMATERIAL UNIT CELL

The effective parameters of the proposed MTM unit cell are extracted utilizing the postprocessing module of CST Microwave Studio. Commonly, the analysis and design of metamaterials incorporate an effective medium model to characterize their external electromagnetic behavior. This approach models the metamaterial as a continuous medium, facilitating simplified analysis and design processes. This particular medium exhibits a notable property of having an effective scalar electric permittivity Ɛeff (ω) and

magnetic permeability μeff (ω) where ω is the angular frequency (Simovski & Tretyakov 2020). Researchers typically utilize the Nicolson-Ross-Weir (NRW) method (Chen et al. 2004) as the most commonly adopted approach to obtain the effective constitutive parameters of metamaterials. D. R. Smith and co-authors used it for the first time in reference (Smith et al. 2002) to describe a metamaterial structure created by a periodic arrangement of wires and split ring resonators.The recovery of the effective electromagnetic constitutive parameters, such as permittivity, permeability, and refractive index of a metamaterial slab, can be achieved by solving the subsequent system of equations, shown in (Musaed et al. 2024).

The MTM design is depicted in Figure 3 , and Table 1 introduces a DNG MTM unit cell. The design features a primary outer square ring on the top layer, serving as the main boundary of the unit cell. Nested within is another square ring at the center, crucial for defining the resonant frequencies of the unit cell and thereby determining its electromagnetic response. At the center of the top layer, a circular ring, along with smaller ones, is integrated. The bottom layer incorporates dual concentric ring ground planes, including an inner ring. These ground planes are instrumental in reflecting waves, thus significantly enhancing the gain and efficiency of the antenna system. The MTM unit cell is constructed with dimensions of 4×4.16 mm² and is fabricated on a Rogers 5880 substrate. This substrate is selected for its superior electromagnetic characteristics, featuring a dielectric constant of 2.2 and a remarkably low loss tangent of 0.0009. With a thickness of 0.787 mm, the separation between the substrate's top and bottom layers is optimized to minimize signal loss, thereby maximizing overall performance.

TABLE 1.Design parameters of the proposed metamaterial

Par.	Dim.(mm)	Par.	Dim.(mm)
L_1	4.16	R_1	1.49
L_2	2.75	R_2	1
L_3	0.616	R_3	0.599
W_1	4	R_4	0.3
W_2	3.8	R_5	1.6
W_3	3.4	R_6	1.2
T	0.8		

Figure 4 illustrates the sequential steps in configuring the double-negative (DNG) metamaterial reflector unit cell. 1 st step the unit cell begins as a simple square ring, establishing the fundamental boundary conditions necessary to define its electromagnetic behavior. 2nd step A circular ring is introduced within the square ring to enhance isotropic properties, ensuring uniform electromagnetic wave interaction. From the back view, a single circular ring starts to form. Final Configuration, the design reaches full complexity, incorporating stacked square and circular rings to achieve precise resonant properties. The back layer features two concentric ring ground planes, optimizing wave reflection and resonance.

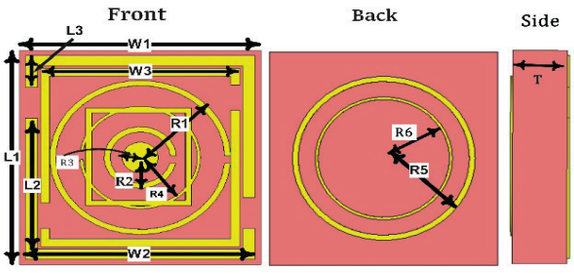

FIGURE 3. Top and bottom views of the proposed MTM unit cell structure.

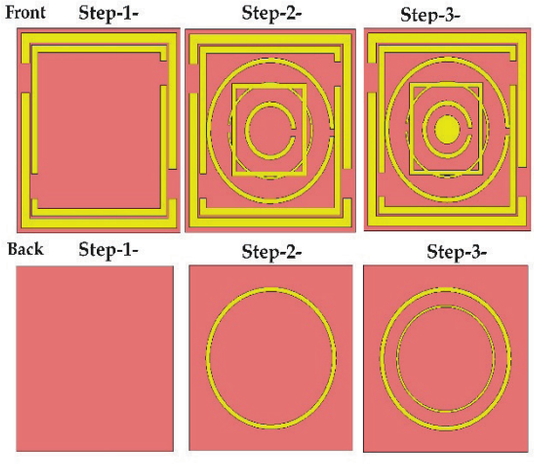

FIGURE 4.Evolution steps for the designed metamaterial.

Figure 5 illustrates the development steps of the proposed metamaterial. In the first step, two square rings with a gap on both sides are added, resulting in a single resonant frequency at 22 GHz with a bandwidth ranging from 21.9 to 23.1 GHz. In the second step, three circular rings are added, along with a square ring at the front and another circular ring at the back. These additions create three resonant frequencies: 21.01 GHz, 25.53 GHz, and 26.44 GHz. These frequencies operate within two distinct bands: the first ranges from 20.99 to 21.3 GHz, and the second ranges from 22.7 to 27.1 GHz. In the third step, a circular element is placed at the center of the square, along with circular rings added to the front section and another ring positioned at the back. This modification creates two resonant frequencies of 23.02 GHz and 26 GHz, resulting in a wide bandwidth that spans from 21.59 GHz to 28.3

GHz. The proposed metamaterial operates in the mm wave range, making it suitable for 5G applications.

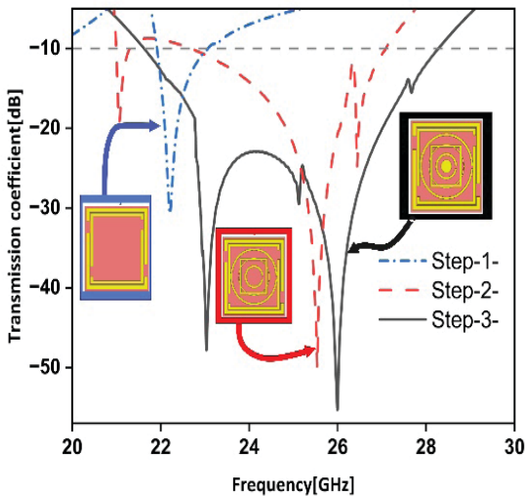

FIGURE 5.Transmission Coefficient Across Design Stages.

Figure 6 illustrates the development of the equivalent circuit for the proposed unit cell. Inductance and capacitance values were optimized using ADS simulation tools. In the circuit, the symbols L1 through L8 denote various inductors formed by the rings, while C1, C2, C3, C4, C5, C7, C8, C9, C10, C11, C12, C13, and C14 represent the capacitors induced by the gaps. Figure 5 (a) illustrates the MTM unit cell's configuration, where the square ring resonator comprises inductive elements L8, L7, L6, and L5. Concurrently, the gaps between these rings introduce capacitive components C14, C13, C12, and C11. In contrast, Figure 6(a) 2 nd step depicts circular rings which generate capacitors C3 through C10 and inductors L4, L3, and L2. It is important to note that the inductors' internal resistances significantly influence the magnitude of the transmission coefficient |S21|. These resistances are omitted in the schematic presented in Figure 6 (b) to streamline the circuit representation. The resonance frequencies are tunable by altering the values of the circuit components, such as the inductors and capacitors. Adjustments to these component values markedly affected the resonance frequencies, which were subsequently fine-tuned to achieve the desired resonances. Figure 7 compares the S21 results obtained from ADS and CST simulations for the proposed metamaterial. While the results differ slightly, the CST simulation exhibits two resonant frequencies at 23.03 GHz and 26 GHz, with an operating bandwidth ranging from 21.5 to 28.3 GHz. In contrast, the ADS simulation shows two resonant frequencies at 24.6 GHz and 26 GHz, operating within two bandwidths 20.4 to 25.7 GHz and 25.8 to 27.8 GHz.

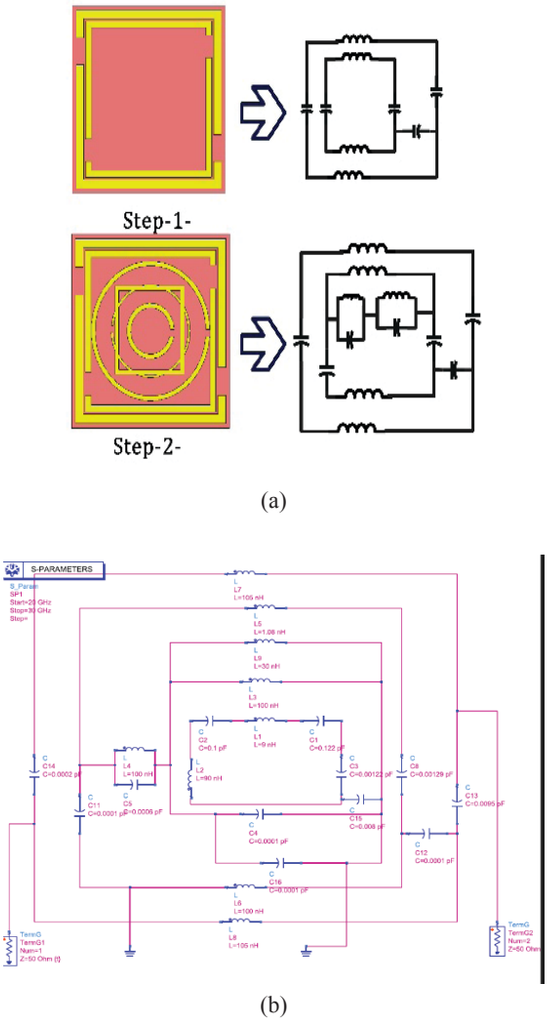

FIGURE 6.Evolution of the equivalent circuit of the unit cell.

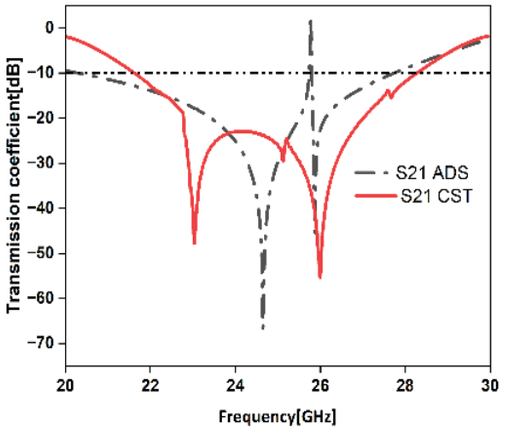

FIGURE 7.ADS and CST simulations of S21 parameters for the proposed metamaterial are compared.

Figure 8 (a) and (b) display the integration of array unit cells into a larger 13 × 10 array, with overall

dimensions of 59.4 × 58.8 × 0.787 mm³. A vector network analyzer (VNA) is used to measure the S-parameters and validate the performance of the proposed metamaterial (MTM) array structure along both the Z and X-axes. whereas the MTM's prototype is positioned between a pair of waveguide ports as depicted in Figure 9. The CST simulations, shown in Figure 10 provide results that extract the real and imaginary components of permittivity, permeability, refractive index, and impedance. These simulations reveal that the analyzed unit cell exhibits the characteristics of a DNG-MTM, with negative values observed for both permittivity and permeability. Notably in Figure 10 (a), the negative permittivity is present within the frequency range of 26.5 to 30 GHz. Additionally, Figure 10 (b) illustrates the negative region of the real part of permeability (μr), spanning from 20 to 28.2 GHz. Moreover, Figure 10 (c) highlights the negative nature of the refractive index (n), with observed limits ranging from 25.1 to 25.2 and 25.8 to 28.2 GHz. These findings provide valuable insights into the electromagnetic properties of the proposed metamaterial unit cell.

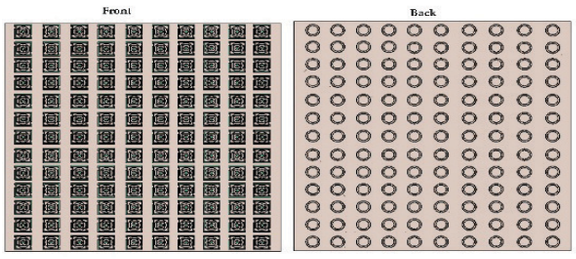

(a)

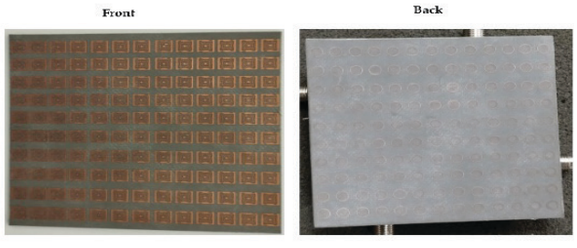

(b)

FIGURE 8.DNG reflector array 13×10 (a) Simulation and (b) Fabrication.

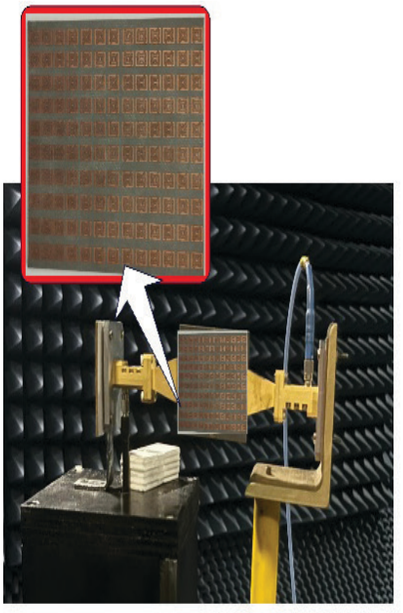

FIGURE 9.Experimental performance measurement setup for the proposed.

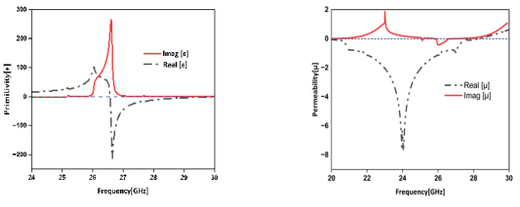

(a) (b)

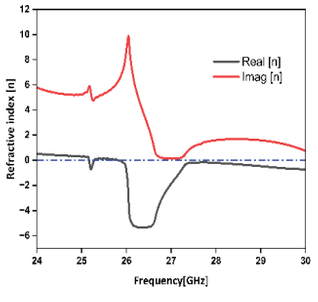

(c)

FIGURE 10.(a) Permittivity ;(b) permeability;(c) refractive index .

The distribution of surface currents in the proposed metamaterial-based structure at 26 GHz is depicted in Figure 11 (a). It reveals that the current mainly gathers along the edges of the nested square rings and the elliptical inner circle. This high concentration of current along the edges can be explained by the edge effect. At high frequencies, electromagnetic waves tend to cluster near

the edges of conductive elements, a behavior dictated by the boundary conditions outlined in Maxwell's equations. This effect boosts surface wave propagation around the edges of the resonant elements, resulting in strong electromagnetic interactions. The electric field distribution for the proposed metamaterial-based structure at 26 GHz is shown in Figure 11(b). You can see that the strongest electric field areas are focused around the elliptical and square resonators, especially along the curved parts of the elliptical ring and the inner edges of the nested square rings. The high intensity of the electric field in these regions is mainly due to resonance effects. This structure supports multiple resonance modes, where the electric field gets tightly confined in certain areas because of constructive interference. The elliptical ring, in particular, helps concentrate the field to its curvature, which leads to a boost in localized field strength. The electric field distribution we see suggests a strong electromagnetic coupling between the various resonant elements. The closeness of the nested structures enhances capacitive effects, which play a part in the observed field confinement. This coupling is essential for determining the effective permittivity of the metamaterial and its capability to manipulate incoming electromagnetic waves.

Figure 11 (c) shows how the magnetic field is distributed in the proposed MTM structure at 26 GHz. The elliptical resonator and the edges of the nested square rings exhibit the strongest magnetic field concentrations. The areas with the highest intensity of the H-field are mainly situated along the curved parts of the elliptical ring and around the square resonators. This pattern indicates that the MTM structure is designed to support strong magnetic resonance at 26 GHz, effectively localizing and amplifying the magnetic field in certain regions. This behavior is typical of metamaterials that are specifically engineered to display DNG properties, where both permittivity and permeability are customized for particular electromagnetic responses.

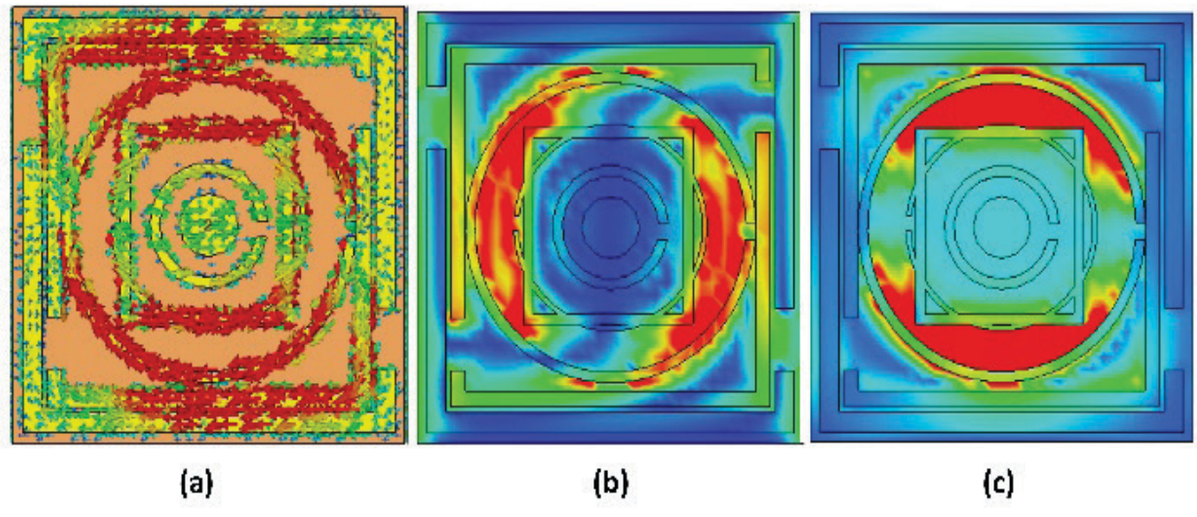

FIGURE 11.(a) Surface current distribution (b) E- field, and (c) H-field.

ANTENNA DESIGN PROCEDURE: SINGLE PORT

SINGLE DESIGN

The modeling process for the antenna design commences by analyzing a single antenna element. Figure 12(a) Step one demonstrates the effect of reducing the rectangular patch's dimensions to 3.4×2.22 mm. This variation leads to different reflection coefficients of -15.58 dB at 24.5 GHz and -12.9 dB at 27.5 GHz. Notably, the frequency response has slightly shifted compared to the original design, and the bandwidth is now assessed from 23.9 GHz to 28.8 GHz. Figure 12(a) step two investigates the consequences of increasing the rectangular patch's dimensions to 5×3.82 mm. This modification yields a different reflection coefficient of -15.5 dB at 22.19 GHz. Similarly, the frequency response experiences a slight shift, and the bandwidth is now measured from 21.6 GHz to 24.6 GHz. By modifying the size of the rectangular patch, the resonant frequency and bandwidth are affected, indicating the sensitivity of the antenna's performance to geometric variations. On the other hand, Figure 12(a) three one shows

the optimized rectangular patch with dimensions of 4.2×3 mm. The antenna design includes an inset feed and a complete ground plane. The reflection coefficient at the resonance frequencies of 23.74 GHz and 28 GHz is evaluated at -27.76 dB and -13.18 dB, respectively. The antenna demonstrates a frequency range spanning from 22.5 GHz to 30 GHz. To study the impact of size variations on the antenna's performance, Figure 12(b) provides a comprehensive comparison of the evolution steps in terms of the reflection coefficient and resonance frequency, Figure 12 (c) provides gain.

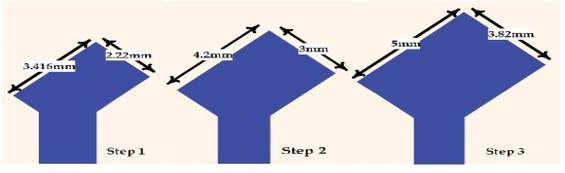

(a)

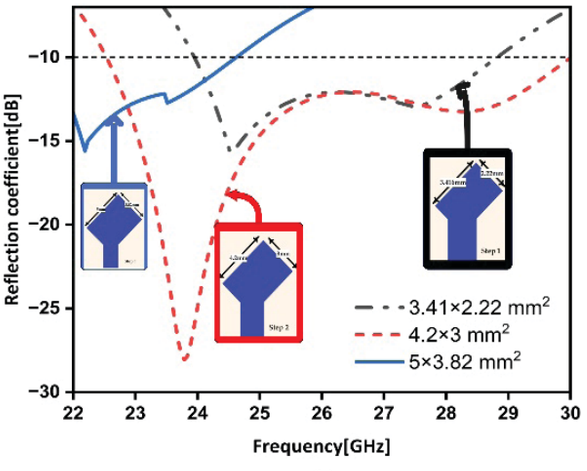

(b)

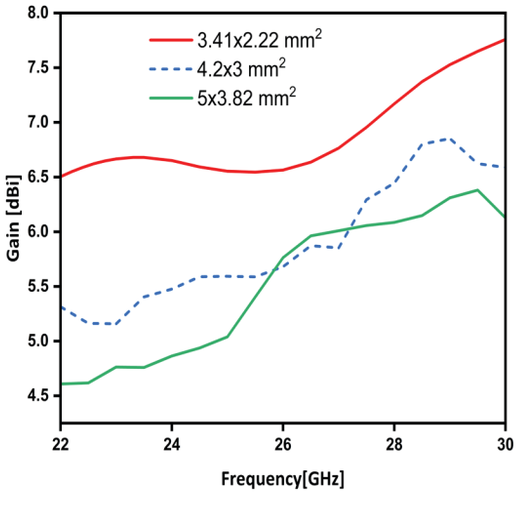

(c)

FIGURE 12.parametric study according to size. (a) Optimizing steps for patch width and length. (b) Reflection coefficient(c) Gain.

ARRAY DESIGN

Figure 11 illustrates the geometry of the 1 × 2 array. Within the array configuration, a power divider is employed and carefully optimized to ensure equal power distribution to each antenna element, thus promoting favorable radiation characteristics. Through this optimization, the gain is elevated to 10 dBi. In contrast, increasing the number of elements to 1×4 results in a noticeable gain enhancement, reaching 14.15 dBi as shown in Figure13(a) and (b). The spacing among these elements is kept at 1.4 mm, which equates to 0.14 of the wavelengths at 28 GHz. This spacing is crucial for preventing interference among the antenna elements, a critical concern in array structures. In the presented design, the challenge at hand is systematically addressed through meticulous adherence to a prescribed spacing of 1.4 mm, coupled with the incorporation of stub feed lines. These stubs serve the critical function of impedance matching between the antenna and the transmission line, thereby enhancing the efficacy of power transfer. The selection of a spacing parameter is purposefully guided by the objective of achieving an optimal z-impedance of 50 ohms, with a zero imaginary part(Moniruzzaman et al. 2021). Furthermore, the stubs are leveraged for precise adjustments to the antenna's resonant frequency and bandwidth, as well as for mitigating cross-polarization effects a necessity in applications necessitating specific polarization orientations.as shown depicted in Figure 14(c)&(d). Further details about the parameters of the array antenna are in Table 2.

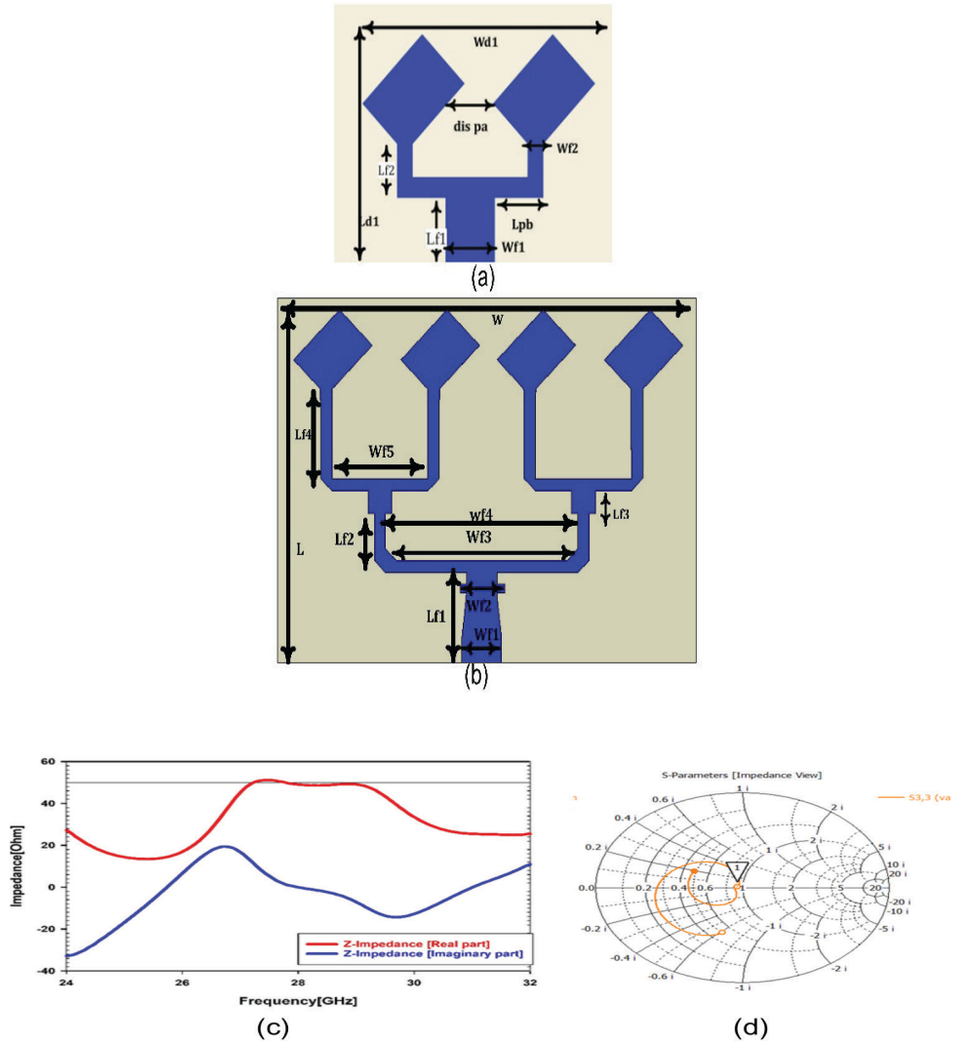

FIGURE 13.Geometry antenna (a) Double element; (b) Four element; (c)Z-impedance (Real and imaginary), and (d) Simth chart.

TABLE 2.Parameters optimized for the proposed design (in millimeters)

Par.	Value	Par.	Value	Par.	Value
For Two Elements					
W_{d1}	17	L_{f1}	2.65	L_{f2}	2.228
L_{d1}	11.7	W_{f1}	2.375	W_{f2}	0.758
dis_{pa}	2.39	L_{bp}	2.327		
For Four Elements					
W	27	Wf3	1.9	Lf1	5.1
L	20.8	Wf4	1.57	Lf2	4.2
Wf1	2.59	Wf5	6.2	Lf3	1.29
Wf2	2.8	Wf6	11.15	Lf4	5.1
For MIMO Elements					
W_{MIMO}	51.6	L_{MIMO}	52.2	S_1	25.2
S_2	27.3	S_3	21.5	S_4	3.1
S_5	0.44	S_6	2.1	L_d	4.6

Figure 14 (a) presents a comparison of the reflection coefficients within the single antenna element, the 1×2 array, and the 1×4 array configurations. In all suggested designs, the reflection coefficient consistently stays below -10 dB. Specifically, for the single antenna element, the reflection coefficient magnitude measures -27.76 dB at 23.74 GHz and -13.1 dB at 27.9 GHz. In contrast, for the 1×2 array, the magnitude of the reflection coefficient is -43.02 dB at 22.7 GHz and -34.02 dB at 27.3 GHz. For the 1×4 array, the magnitude of the reflection coefficient is -24.05 dB, observed at 28.3 GHz within the desired frequency band. Based on the -10 dB criteria, the observed bandwidths are as follows: 22.55-30 GHz for the single element, spanning a dual-band from 21.1 -23.6 GHz, and 26.47-30 GHz for the two and four-element array antennas, respectively.It is notable that the incorporation of an array structure in the antenna design entails a slight reduction in bandwidth, primarily attributable to the inclusion of a power divider. This results in marginal losses during the excitation of individual antenna elements. However, this challenge has been effectively addressed through the implementation of tapered feed lines, leading to a notable enhancement in bandwidth (Pozar 2021).

The values presented in Figure 14(b) compare the gain of single, double, and four-element antenna arrays. The gain value for a single element is 6.53 dBi, for a double-element array it is 10.2 dBi, and for a four-element array, it is 14.1 dBi. The observed differences in gain values are primarily due to the array factor, which enhances the overall directivity and gain of the antenna system(Haupt 2010). In a single-element antenna, the gain is solely dependent on the individual element's characteristics. However, when multiple elements are combined into an array, the constructive interference of the radiated waves from each element results in increased directivity and thus higher gain. In a double-element array, the gain increases to 10.2 dBi because the elements are phased in a manner that their radiation patterns combine constructively, leading to a narrower beamwidth and higher directivity. Similarly, in a four-element array, the gain further increases to 14.1 dBi as the array configuration allows for even more constructive interference and a further narrowed beamwidth, resulting in a significant boost in directivity and gain .

(a) (b)

FIGURE 14.(a) reflection coefficient (b) gain

ANTENNA DESIGN PROCEDURE MULTI-PORT

The design is further advanced to achieve Multiple-Input Multiple-Output capability. Figure 16(a) and Table 2 illustrates the addition of four array elements to its substrate with dimensions of 52.1 × 51.5mm2, distributed in a mutually orthogonal manner with a separation angle of 90 degrees to reduce interference between elements (Leshem & Erez 2021). The distance between the edges of the elements is 4.6 mm. A parametric study was performed on the element spacing, where 4.6 mm was identified as the optimal distance. This spacing achieves the best isolation

performance by minimizing mutual coupling while maintaining a compact antenna array suitable for 5G mmWave applications. To enhance performance, slots are added to the design ground behind the power feeding networ. As for Figure 15(b), they demonstrate the addition slots in the design ground aimed at improving isolation between elements. Slots in the ground plane can disrupt the continuity of the current paths, thereby reducing the coupling between adjacent elements. also, can act as reactive loads, altering the impedance characteristics of the ground plane. By strategically placing slots, the impedance seen by each antenna element can be modified and can help to absorb these surface waves, preventing them from coupling energy between adjacent elements and the Slots effectively increase the physical distance between different parts of the ground plane. This increased separation can reduce the electromagnetic coupling between antenna elements, leading to improved isolation(Sufian et al. 2021).

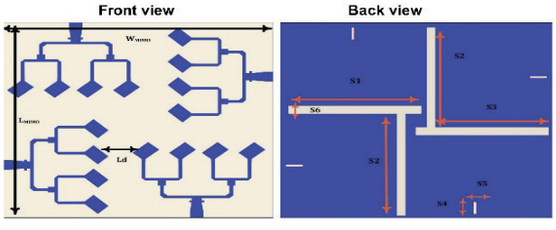

FIGURE 15.Layout of MIMO antenna: (a) front, (b) back.

To improve the gain of MIMO antennas for millimeter-wave applications, a proposed configuration integrating metamaterial elements is presented in Figure 16. The MIMO antenna system includes a DNG reflector positioned 5 mm behind, which effectively reflects backward waves and facilitates strong interaction between reflected and forward waves, resulting in a notable gain within the operating band. Metamaterial, employed within this design, possesses the capability to manipulate the phase of incident electro-magnetic waves. Through a meticulously devised metamaterial structure, precise control over the phase of radiated waves is achievable, facilitating constructive interference in desired directions. This controlled phase distribution enables effective beam steering, directing the antenna radiation towards specific angles of interest and consequently augmenting gain in those directions. Additionally, metamaterial facilitates the focusing of radiated energy, resulting in a more concentrated beam, thereby further enhancing antenna performance.

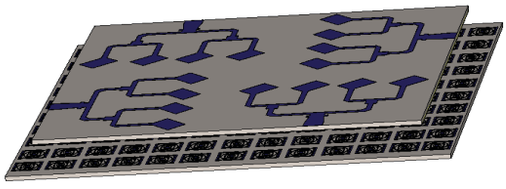

FIGURE 16.MIMO antenna integrated with metamaterial DNG reflectors.

EXPERIMENTAL RESULTS

The designed MIMO antenna has been simulated using CST and fabrication has been done to verify is performance. Port measurements were carried out utilizing a vector network analyzer (VNA), as illustrated in Figure 17.

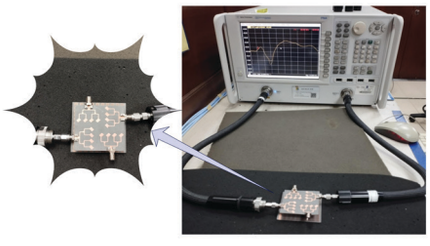

FIGURE 17. Experimental arrangement for the MIMO antenna measurement.

S-PARAMETER

The simulation of S-parameters for a Multiple-Input Multiple-Output (MIMO) antenna system, with and without the presence of metamaterial (MTM), has been investigated. The MIMO antenna operates within the frequency range of 25.69 to 34 GHz. Upon integrating an MTM decoupling structure alongside the antennas, the operational bandwidth extends by 200 MHz, as depicted in Figure 18(a). In the absence of the DNG reflector, a notable mutual coupling of -27.1 dB was observed between elements positioned opposite each other. However, the inclusion of the double-negative (DNG) reflector decoupling structure effectively mitigated mutual coupling, resulting in an improved isolation of 31.3 dB between MIMO elements, as illustrated in Figure 18(b). In contrast, Figure 18(c) presents the simulated reflection coefficients of the proposed design with a DNG reflector, which measured -27.5 dB and -37.5 dB at 26.9 GHz and 28.2 GHz, respectively. Actual measurements yielded values of -29.4 dB and -34.5 dB at 26.5 GHz and 27.6 GHz, respectively. Additionally, Figure 18(d) illustrates both simulated and measured transmission coefficients of the

proposed design with (DNG) reflector, which measured -31.3 dB and -32.7 dB, respectively. The observed larger isolation in real-world MIMO antenna setups compared to simulations may be attributed to several factors. Real-world measurement environments introduce additional sources of isolation, such as electromagnetic interference from nearby objects, crosstalk from cables or connectors, and reflections from surrounding surfaces, which are not fully captured in simulations.

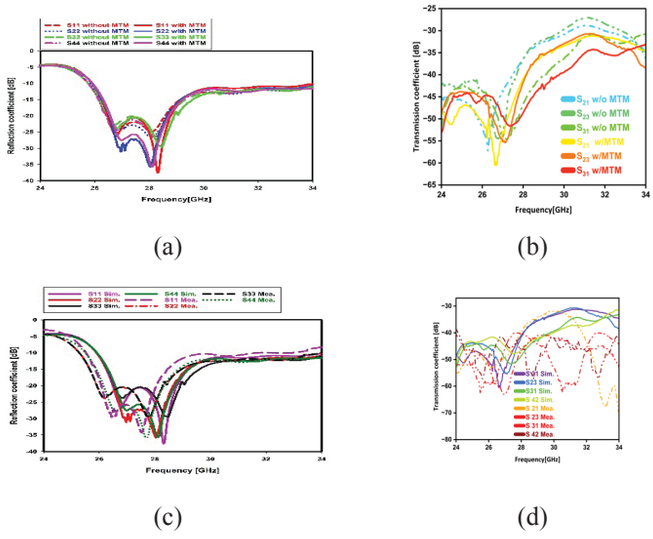

FIGURE 18.(a) Reflection coefficient, (b) transmission coefficient for MIMO antenna element, (c) simulated and measured reflection coefficient, (d) the transmission coefficient was simulated and measured.

GAIN AND EFFICIENCY

In Figure 19(a), the gain values before and after the addition of the (DNG) reflector are depicted. The gain was initially 14 dBi, which increased to 14.3 dBi after incorporating the (DNG) reflector. This enhancement in the operating frequency range is attributed to the (DNG) reflector's ability to reduce losses associated with impedance mismatch and surface currents. Figure 19(b) illustrates the change in efficiency, which increased to 97% after the (DNG) reflector was introduced. Conversely, Figure 19(c) demonstrates the measured gain values in the laboratory, indicating a decrease due to manufacturing losses, measurement devices, and cables. Finally, Figure 19(d) presents the efficiency values measured in the laboratory, which decreased to 94% for the same reasons.

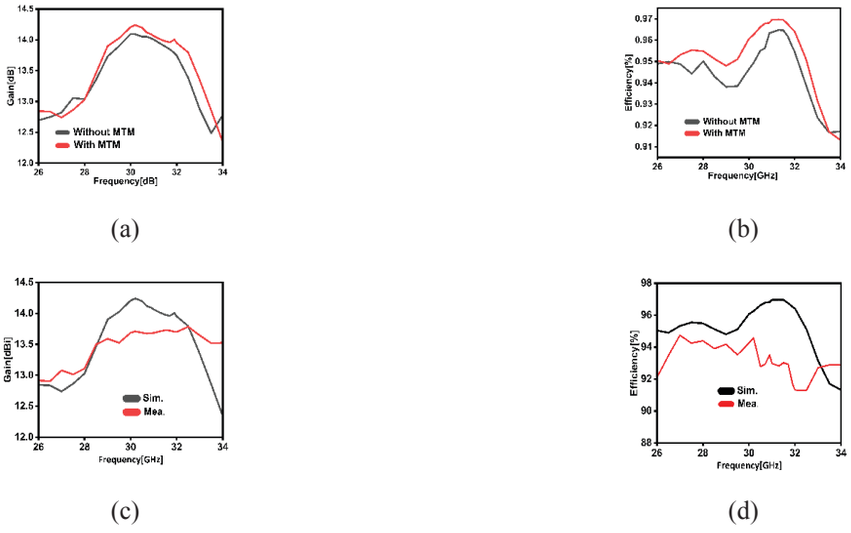

FIGURE 19.(a) & (b) Gain and efficiency for MIMO antenna with and without the use of metamaterial, (c) & (d) simulated and measured the gain and efficiency of the proposed design.

SURFACE CURRENT

To understand how the metamaterial works in reducing the mutual coupling by suppressing surface waves, the distribution of surface current at 28 GHz will be investigated. Figure 20 represents the surface current distribution of the Multiple-Input Multiple-Output (MIMO) antenna design. In this figure, antenna 1 is excited while the other antennas are terminated with a 50-Ω load. Without the DNG reflector, Figure20(a), there is an obvious mutual coupling current seen at the neighboring antenna at 28 GHz when antenna 1 is excited. But when a DNG (Double Negative) reflector is applied, as seen in Figure 20(b), the isolation between adjacent antennas gets better. The effect of enhancing this isolation is by decreasing the mutual coupling between the neighboring fields. The presence of the DNG reflector changes the current distribution on the antenna surface due to interactions between incident waves and the metamaterial.

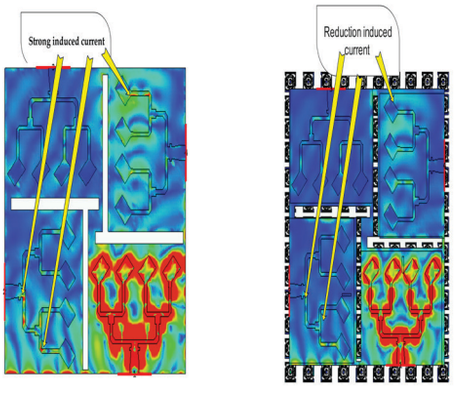

FIGURE.20.Surface current of the designed antenna.

RADIATION PATTERN

Through a combination of measurement data and simulation, Figure 21 showcases the radiation patterns of port 1 within the antenna system. This figure provides a visual representation of the E-plane radiation patterns along the YZ and XZ axes, specifically at a defined azimuthal angle (phi = 90°; 0°), as well as the H-plane radiation patterns at a specific polar angle (theta = 90°) for port 1. These patterns were observed at a frequency of 28 GHz. Upon analyzing the far-field observations, it becomes clear that the primary beam is perpendicular to the antenna, displaying distinct directional characteristics in both the YZ and XZ planes. For a comprehensive evaluation, Table 2 presents various performance metrics such as gain, bandwidth, and isolation.

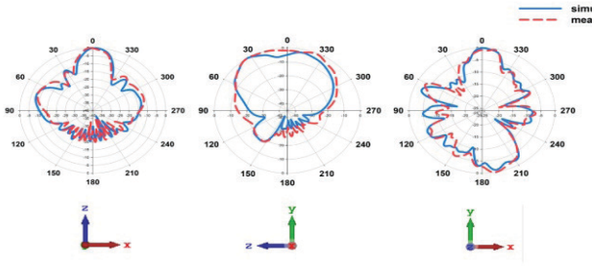

FIGURE 21.Radiation pattern of the designed antenna.

MACHINE LEARNING FOR ANTENNA DESIGN EVALUATION

In the last ten years, among many other aspects, the integration of machine learning techniques (ML), a subfield of Artificial Intelligence (AI), in antenna design has been important since it is possible for ML to learn and predict from simulated antenna data through well-structured training processes. Many researchers have adopted ML-based regression prediction models for validating antenna performance to ensure gains, which are some of the most important parameters, in a more reliable and repeatable way (Haque, Saha, et al. 2023; Haque, Zakariya, Al-Bawri, et al. 2023; Wei 2023). In this work, machine learning is used to predict the gain of a MIMO array antenna and compare the ML predicted values to the real gain realized by CST simulation (ground-truth). By comparison, we seek to assess if CST produces gains close to those expected.

The first phase in implementing this machine learning approach is collecting relevant data, which is critical because any machine learning model needs good data on which to learn. It begins with the design of the MIMO array antenna and several parametric sweeps (Haque, Zakariya, Singh, et al. 2023) on critical design elements such as slot and stub dimensions, ground plane, and feedline. These parameters are known to significantly affect the antenna's performance, and their systematic variation contributes to a good volume of data. The size of the problem's difficulty, input features' dimensionality, and how high-level ML model selected determines how much larger volumes of data could improve predicting the right output. Therefore, we generated 200 data samples through simulations using CST Microwave Studio (CST MWS) to enable the second phase, which is the application of regression-based machine-learning algorithms for the extrapolation of realized gain of the antenna. Following best practices (Nguyen et al. 2021), the dataset is divided into two parts, 80% is for training the ML predictor models and 20% is to test the learned ML models. For each model, we used

the standard implementations available in Python's scikit-learn libraries, with standard hyperparameters of the library. After this, the ML algorithms are implemented for predictions of antenna gain values. The schematic diagram in Figure 22 illustrates the phases of ML process. This research investigates the following six distinct machine learning models: support vector regression, logistic regression, linear regression, random forest regression, decision tree regression, and XGBoost regression. These algorithms are selected based on their ability to effectively carry out nonlinear regression tasks, which are typical in advanced antenna design specifications. For this application, one of the most appropriate techniques remains regression models because of their capability to output numerical values accurately (Talpur et al. 2023).

All machine learning algorithms implementations, training, and testing were carried out using Google Colab, a cloud-based Python simulation environment. Performance of these ML models is assessed using several statistical measurements. Some major metrics are R^2, variance score, mean squared error (MSE), mean absolute error (MAE) and mean squared logarithmic error (MSLE). They give an insight into how well the model is working and what might need to be improved. For a loss function in regression tasks (commonly employed), the mean squared error is computed by taking an average of the squared differences in actual/predicted values over all data point (Haque, Saha et al. 2023).

Table 3 depicts and compares the performance of the ML models using the evaluation metrics. For the Support Vector Regression (SVR) model, the MAE, MSE, and MSLE scores are among the lowest at 0.0403, 0.00353, and 0.000045. Moreover, SVR has an R-squared value of 96.7971% and a variance score of 96.1972%, which is very good in terms of predictive accuracy. Likewise, XGB Regression Model gives an excellent performance having slightly higher MAE, MSE and MSLE values at 0.0422, 0.00381 and 0.00075 respectively with an R-squared of 96.1283% and a variance score of 96.0397%. The Random Forest Regression model is, admittedly, less accurate than both XGBoost and SVR. However, it still performs robustly: MAE 0.05312, MSE 0.00525, MSLE 0.00062. Its R-squared for the test data is at 95.9233%, and the variance score is 95.8822% reliable in its predictive abilities. Model suitability can also be confirmed by looking at the close alignment between predicted results and simulation results. Figure 23 shows the difference between the simulated and projected gains for SVR & XGB for a set of 23 test samples. In addition, the average incorrectness rate does not exceed 4%. All of the available Regression models report an accuracy of 90% or above. Since the predicted result is so similar to the simulated result, this suggests both methods are robust and accurate, reinforcing the reliability of our results. The agreement between the simulation-based and ML-based approaches further validates our conclusions. Machine learning delivers powerful results but faces challenges such as dependence on large, high-quality datasets, vulnerability to bias and noise, limited interpretability, poor generalization to new conditions, high computational demands, and susceptibility to adversarial attacks—necessitating robust data management, validation, transparency, and governance.

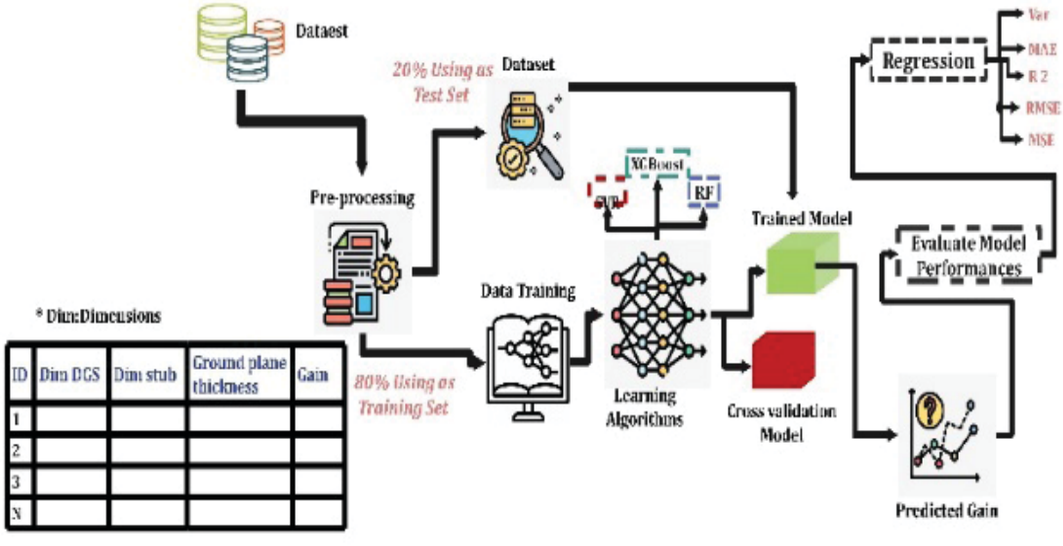

FIGURE 22.Schematic diagram of machine learning-based prediction for MIMO antenna design.

TABLE 3.Performance metrics of ML regressors for gain

No.	Algorithms	Var	R^2	MSLE	MAE	MSE
1	Support Vector Regression	96.1972%	96.7971%	0.000045	0.0403	0.00353
2	XGB Regression	96.0397%	96.1283%	0.00075	0.0422	0.00381
3	Random Forest Regression	95.8822%	95.9233%	0.00062	0.05312	0.00525
4	Decision Tree Regression	94.6339%	94.8762%	0.00056	0.05922	0.00958
5	Logistic Regression	92.3762%	92.6822%	0.00068	0.07448	0.01002
6	Linear Regression	90.2339%	90.6283%	0.00049	0.09191	0.01009

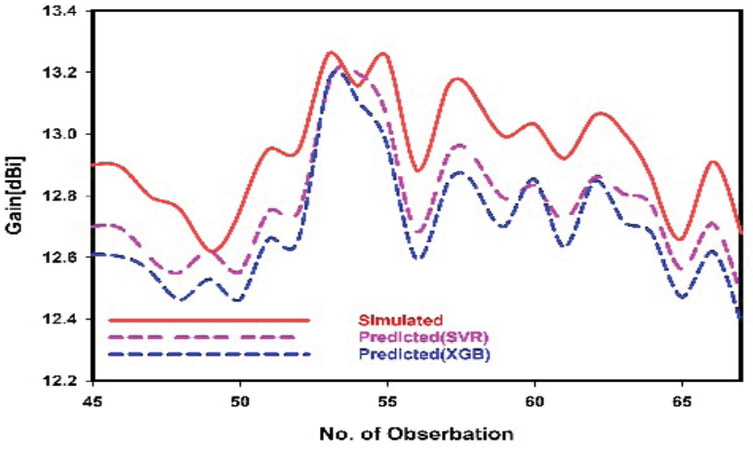

FIGURE 23.Simulated vs predicted Gain using support vector & XGB regression.

COMPARISON WITH EXISTING WORKS AND REAL-WORLD INTEGRATION POTENTIAL

Table 4 shows the qualitative improvements over previous designs in addition to the quantitative superiority of the suggested design in terms of gain, bandwidth, and isolation. Our method incorporates a DNG metamaterial reflector, ground-plane slots, and a 4x4 sub-array per port, in contrast to many previous designs that depended on larger physical dimensions or simpler decoupling techniques. Without compromising compactness, this dual enhancement mechanism simultaneously increases gain and isolation. For instance, the suggested antenna achieves a much higher gain (14.3 dBi vs. ≤9.53 dBi) while maintaining excellent isolation (>32 dB) in a footprint that can be integrated into portable devices, in contrast to other metamaterial-based MIMO designs [36, 38]. Our structure provides more robust isolation and a wider bandwidth compared to DGS-only designs [37]. demonstrating that metamaterial-assisted engineering can outperform traditional decoupling approaches. The implementation of machine learning verification further distinguishes our work, ensuring predictive reliability and paving the way for faster design iterations.

Beyond laboratory validation, the proposed antenna is well-suited for real-world deployment in mmWave 5G systems. Its compact geometry (52.1 × 51.5 × 0.787 mm^3) facilitates integration into mobile devices, small-cell base stations, and IoT terminals where space is constrained. The orthogonal element arrangement and high isolation help sustain performance even in scenarios where devices are held close to the human body, reducing detuning effects from tissue proximity. Furthermore, the use of Rogers 5880 substrate with low dielectric loss ensures stable performance when enclosed within common device housings such as polycarbonate or ABS plastics, where dielectric loading could otherwise degrade bandwidth and efficiency.

TABLE 4. Reported studies performance with the proposed MIMO antenna

Ref	Technique	Freq (GHz)	Gain (dBi)	B.W (GHz)	Isolation (dB)	NO. Element	No. of Port	Edge to edge (mm)	Dimension (mm^3)	ML verification
(Dixit & Kumar 2020)	MTM	28	9.53	4.5	--	1	1	-	FR4- 40×24×1.6	NO
(Khalid et al. 2020)	Defected Ground Structure (DGS)	28	8.3	4.1	≥-17	2	4	10.7	30 × 35 × 0.76 Rogers R04350B	NO
(Esmail & Koziel 2023)	MTM	28	5.5	3.3	>-18	2	2	--	26×14.5 ×0.508 Rogers RT5880	NO
(Mulla et al. 2021)	DGS and Ms	28	6.28	3.1	-18.86	12	12	5.357	62 × 62 ×0.787 Rogers RT5880	NO
(Sultan et al. 2020)	Ms ; and slot	28	11	4	-40	8	8	-	100 × 60 ×0.2 Rogers RO 4003C	NO
(Zhu et al. 2018)	Antipodal Vivaldi antenna (AVA)	24. 28.5	11.2	4.1	>-10	8	1	5	28.823 × 60 × 0.787	NO
(Murthy 2020)	Metamaterial	28	5.6	2.59	-16	1	4	-	20 × 40×1.6 Rogers RT5880	NO
(Al Abbas et al. 2019)	Slot antenna	28	5.1	5	≥ -17	4	4	-	158 × 77.8×0.301 RT/duroid-5880	NO
(Alanazi & Khamas 2022)	Dielectric Resonator	28	9.5	5	-15	1	2	-	25 ×15×0.25 RT/duroid-5880	NO
(Cuneray et al. 2023)	Slot	28	8.14	3.05	>30	1	4	-	60 × 60 ×0.508 RT/duroid-5880	NO
Proposed design	Ms and slot in ground	28	14.3	8.06	≥ -32.7	16	4	4.6	52.1×51.5×0.787 RT/duroid-5880	Yes

*MTM: Metamaterial, Ms: Metasurface.

CONCLUSION

A compact four-port orthogonal MIMO antenna for mmWave 5G applications was presented in this paper. It was improved with a double-negative metamaterial reflector to provide better isolation, gain, and bandwidth. For further decoupling, each port incorporates a 4x4 sub-array on a Rogers 5880 substrate with ground-plane slots that are optimized. Excellent agreement between simulated and measured results is demonstrated by the design, which has a wide operating bandwidth of 8.06 GHz, a peak gain of 14.3 dBi, isolation exceeding 32 dB, and radiation efficiency up to 97%.Compared with previous works, the proposed antenna offers a unique combination of high performance and compact size, enabling easy integration into portable devices and base stations. The use of machine learning regression models for performance prediction further validates the design's reliability and facilitates faster optimization in future implementations. These results confirm the proposed antenna as a strong candidate for next-generation mmWave 5G systems requiring high capacity, low interference, and robust operation in real-world deployment scenarios. Future work could focus on integrating beamforming techniques, evaluating thermal effects on performance, and extending the design to 6G frequency bands.

ACKNOWLEDGEMENT

The authors would like to thank Universiti Kebangsaan Malaysia for the financial aid in supporting this work.

DECLARATION OF COMPETING INTEREST

None.

REFRENCE

Al-Bawri, S. S., Ananta, R. A., Haque, M. A., Abdulkawi, W. M., Singh, N., Jilani, M. a. K., Paul, L. C. & Aljaloud, K. 2024. Machine learning technique based highly efficient slotted 4-port MIMO antenna using decoupling structure for sub-THz and THz 6G band applications. *Optical and Quantum Electronics* 56(10): 1611.

Al Abbas, E., Ikram, M., Mobashsher, A. T. & Abbosh, A. 2019. MIMO antenna system for multi-band millimeter-wave 5G and wideband 4G mobile communications. *IEEE Access* 7: 181916-181923.

Alanazi, M. D. & Khamas, S. K. 2022. A compact dual band MIMO dielectric resonator antenna with improved performance for mm-wave applications. *Sensors* 22(13): 5056.

Banday, Y., Mohammad Rather, G. & Begh, G. R. 2019. Effect of atmospheric absorption on millimetre wave frequencies for 5G cellular networks. *IET Communications* 13(3): 265-270.

Bang, J. & Choi, J. 2018. A SAR reduced mm-wave beam-steerable array antenna with dual-mode operation for fully metal-covered 5G cellular handsets. *IEEE Antennas and Wireless Propagation Letters* 17(6): 1118-1122.

Chen, L.-F., Ong, C. K., Neo, C., Varadan, V. V. & Varadan, V. K. 2004. *Microwave electronics: measurement and materials characterization.* John Wiley & Sons.

Cuneray, K., Akcam, N., Okan, T. & Arican, G. O. 2023. 28/38 GHz dual-band MIMO antenna with wideband and high gain properties for 5G applications. *AEU-International Journal of Electronics and Communications* 162: 154553.

Dixit, A. S. & Kumar, S. 2020. The enhanced gain and costвЂђeffective antipodal Vivaldi antenna for 5G communication applications. *Microwave and Optical Technology Letters* 62(6): 2365-2374.

El-Nady, S., Elsharkawy, R. R., Afifi, A. I. & Abd El-Hameed, A. S. 2021. Performance improvement of substrate integrated cavity fed dipole array antenna using ENZ metamaterial for 5G applications. *Sensors* 22(1): 125.

El Houda Nasri, N., El Ghzaoui, M., Das, S., Jackson, B., Madhav, B. T. P. & Fattah, M. 2024. A square split ring resonator-based metamaterial integrated high gain 4вЂ‰Г—вЂ‰4 MIMO antenna with circular polarization for wideband 5G millimeter-wave applications. *Optical and Quantum Electronics* 56(6): 971.

Esmail, B. A. & Koziel, S. 2023. High isolation metamaterial-based dual-band MIMO antenna for 5G millimeter-wave applications. *AEU-International Journal of Electronics and Communications* 158: 154470.

Haque, M. A., Saha, D., Al-Bawri, S. S., Paul, L. C., Rahman, M. A., Alshanketi, F., Alhazmi, A., Rambe, A. H., Zakariya, M. & Hashwan, S. S. B. 2023. Machine learning-based technique for resonance and directivity prediction of UMTS LTE band quasi Yagi antenna. *Heliyon* 9(9):

Haque, M. A., Zakariya, M., Al-Bawri, S. S., Yusoff, Z., Islam, M., Saha, D., Abdulkawi, W. M., Rahman, M. A. & Paul, L. C. 2023. Quasi-Yagi antenna design for LTE applications and prediction of gain and directivity using machine learning approaches. *Alexandria Engineering Journal* 80: 383-396.

Haque, M. A., Zakariya, M. A., Singh, N. S. S., Rahman, M. A. & Paul, L. C. 2023. Parametric study of a dual-band quasi-Yagi antenna for LTE application. *Bulletin of Electrical Engineering and Informatics* 12(3): 1513-1522.

Haupt, R. L. 2010. *Antenna arrays: a computational approach.* John Wiley & Sons.

Imam-Fulani, Y. O., Faruk, N., Sowande, O. A., Abdulkarim, A., Alozie, E., Usman, A. D., Adewole, K. S., Oloyede, A. A., Chiroma, H., Garba, S., Imoize, A. L., Baba, B. A., Musa, A., Adediran, Y. A. & Taura, L. S. 2023. 5G Frequency Standardization, Technologies, Channel Models, and Network Deployment: Advances, Challenges, and Future Directions. *Sustainability* 15(6):

Iqbal, A., Basir, A., Smida, A., Mallat, N. K., Elfergani, I., Rodriguez, J. & Kim, S. 2019. Electromagnetic bandgap backed millimeter-wave MIMO antenna for wearable applications. *IEEE Access* 7: 111135-111144.

Khalid, M., Iffat Naqvi, S., Hussain, N., Rahman, M., Fawad, Mirjavadi, S. S., Khan, M. J. & Amin, Y. 2020. 4-Port MIMO antenna with defected ground structure for 5G millimeter wave applications. *Electronics* 9(1): 71.

Leshem, A. & Erez, U. 2021. The interference channel revisited: Aligning interference by adjusting antenna separation. *IEEE Transactions on Signal Processing* 69: 1874-1884.

Mandloi, M. S., Gupta, P., Parmar, A., Malviya, P. & Malviya, L. 2023. Beamforming MIMO array antenna for 5G-millimeter-wave application. *Wireless Personal Communications* 129(1): 153-172.

Moniruzzaman, M., Islam, M. T., Misran, N., Samsuzzaman, M., Alam, T. & Chowdhury, M. E. H. 2021. Inductively tuned modified split ring resonator based quad band epsilon negative (ENG) with near zero index (NZI) metamaterial for multiband antenna performance enhancement. *Sci Rep* 11(1): 11950.

Mulla, M., Sohail, M., Ulusoy, A. H., Uyguroдџlu, R., Rizaner, A. & Amca, H. 2021. A single user millimeter wave massive MIMO system using defected ground structure and metasurface antenna arrays. *2021 29th Signal Processing and Communications Applications Conference (SIU)*, pp.1-4.

Murthy, N. 2020. Improved isolation metamaterial inspired mm-Wave MIMO dielectric resonator antenna for 5G application. *Progress In Electromagnetics Research C* 100: 247-261.

Musaed, A. A., Al-Bawri, S. S., Aljaloud, K., Abdulkawi, W. M., Islam, M. T., Singh, M. J., Sakawi, Z. & Ibrahim, H. H. 2024. A symmetric TH shape wideband negative index metamaterial for 28-GHz millimeter-wave applications. *Journal of Magnetism and Magnetic Materials* 589: 171520.

Nguyen, Q. H., Ly, H.-B., Ho, L. S., Al-Ansari, N., Le, H. V., Tran, V. Q., Prakash, I. & Pham, B. T. 2021. Influence of data splitting on performance of machine learning models in prediction of shear strength of soil. *Mathematical Problems in Engineering* 2021(1): 4832864.

Omar, M. F. M., Zubir, I. A., Kamal, S., Rajendran, J. A., Mohamed, J. J., Ahmad, Z. A., Ain, M. F. & Rahim, S. K. A. 2024. A critical review on the development of multi-geometrical stacked wideband dielectric resonator antenna. *Alexandria Engineering Journal* 100: 111-141.

Pozar, D. M. Microwave Engineering, copyright 2012 by John Wiley & Sons. *Inc*:

Pozar, D. M. 2021. *Microwave engineering: theory and techniques.* John wiley & sons.

Rai, A., Singh, D. K., Sehgal, A. & Cengiz, K. 2023. *Paradigms of Smart and Intelligent Communication, 5G and Beyond.* Springer.

Rappaport, T. S., Sun, S., Mayzus, R., Zhao, H., Azar, Y., Wang, K., Wong, G. N., Schulz, J. K., Samimi, M. & Gutierrez, F. 2013. Millimeter wave mobile communications for 5G cellular: It will work! *IEEE Access* 1: 335-349.

Saad, A. a. R. & Mohamed, H. A. 2019. Printed millimeter-wave MIMO-based slot antenna arrays for 5G networks. *AEU-International Journal of Electronics and Communications* 99: 59-69.

Sehrai, D. A., Asif, M., Shah, W. A., Khan, J., Ullah, I., Ibrar, M., Jan, S., Alibakhshikenari, M., Falcone, F. & Limiti, E. 2021. Metasurface-based wideband MIMO antenna for 5G millimeter-wave systems. *IEEE access* 9: 125348-125357.

Simovski, C. & Tretyakov, S. 2020. *An introduction to metamaterials and nanophotonics.* Cambridge University Press.

Singh, M. J., Saleh, W. W., Abed, A. & Fauzi, M. 2023. A review on massive MIMO antennas for 5G communication systems on challenges and limitations. *Jurnal Kejuruteraan* 35(1): 95-103.

Smith, D. R., Schultz, S., Markoš, P. & Soukoulis, C. 2002. Determination of effective permittivity and permeability of metamaterials from reflection and transmission coefficients. *Physical review B* 65(19): 195104.

Song, J., Castellanos, M. R. & Love, D. J. 2017. 10 Millimeter Wave Communications for 5G Networks. *Key Technologies for 5G Wireless Systems*: 188.

Sufian, M. A., Hussain, N., Askari, H., Park, S. G., Shin, K. S. & Kim, N. 2021. Isolation enhancement of a metasurface-based MIMO antenna using slots and shorting pins. *IEEE access* 9: 73533-73543.

Sultan, K. S., Abdullah, H. H., Abdallah, E. A. & El-Hennawy, H. S. 2020. Metasurface-based dual polarized MIMO antenna for 5G smartphones using CMA. *IEEE Access* 8: 37250-37264.

Talpur, M. a. H., Khahro, S. H., Ali, T. H., Waseem, H. B. & Napiah, M. 2023. Computing travel impendences using trip generation regression model: A phenomenon of travel decision-making process of rural households. *Environment, Development and Sustainability* 25(7): 5973-5996.

Tariq, S., Naqvi, S. I., Hussain, N. & Amin, Y. 2021. A metasurface-based MIMO antenna for 5G millimeter-wave applications. *IEEE Access* 9: 51805-51817.

Wei, Z. 2023. Machine Learning-Assisted Automated Modeling, Optimization and Design of Electromagnetic Devices.

Zhu, S., Liu, H., Chen, Z. & Wen, P. 2018. A compact gain-enhanced Vivaldi antenna array with suppressed mutual coupling for 5G mmWave application. *IEEE Antennas and Wireless Propagation Letters* 17(5): 776-779.